Vol. **111** (2007) *ACTA PHYSICA POLONICA A* No. 3

Three-Colour Excitation of D_1 Transition in Cold Rubidium Atoms

A.M. Alhasan

Institute of Physics, Faculty of Mathematics and Natural Sciences
Pomeranian University in Słupsk
Arciszewskiego 22b, 76-200 Słupsk, Poland

(Received April 3, 2006; revised version October 13, 2006; in final form March 19, 2007)

We analyse the three-colour electromagnetically induced transparency for the D_1 transition in cold ^{87}Rb atoms. We report an enhancement of the electromagnetically induced emission of a drive field as an exclusive enhancement of the third- and fourth-rank components of the density matrix. Moreover, the gain experienced by the drive field is attributed to the influence of the quantum switching effect on the increased absorption of the probe field. The electromagnetically induced emission effect is employed to generate slow light Gaussian-wave trains with shape preserving. These soliton trains were not only generated in the drive channel as has been designated but also in the switch channel which reveals multiple-light storage phenomenon.

PACS numbers: 42.50.Gy, 42.50.Hz, 42.65.–k

1. Introduction

Recently, the coherent interaction of laser light with multi-level atoms has revealed new features and modern optical spectroscopic techniques for cold and hot atoms confined in magneto-optical trap (MOT), Bose–Einstein condensate (BEC) and rare-earth doped solids. Among these new features which we have concerned with, are the electromagnetically induced transparency (EIT) [1], the quantum switching effect in cold gases [2–4] and in solids [5]. Out of a variety of those modern spectroscopic techniques we are going to mention briefly the following ones: the three-photon electromagnetically induced transparency [6], the observation of doubly dressed state [7], and the experimental demonstration of laser oscillation without population inversion via quantum interference [8]. That will assist us in controlling the group velocity in cold atoms [9, 10] as well as the developing optical memory devices and optical switches (cf. [5] and references therein). In recent papers, we have analysed the quantum interference effect in the two-

-colour excitation of the sodium atom and the time dependent features of the two--colour pulse propagation [11–13]. We have found that during the time dependent excitations, the coupling field enhances under the two-photon EIT condition. In addition, the rubidium (^{85}Rb) atomic vapour in the three-photon EIT experiment has been driven by two coherent fields, which are, in contrast, continuous [6]. The drive field either detuned from D_1 or D_2 lines while the probe is being nearly resonant with the one of the atomic transitions. In the present paper, we will deal with the N type configuration in which three electromagnetic fields interact with the four allowed dipole transitions within the same manifold of the D_1 line in ^{85}Rb. We have restricted ourselves to the sharp line case that is adequate for cold atoms. Our goal is to illustrate the dependence of the absorption/gain of the radiation fields on their intensities and the relaxation rates both radiational and collisional. We shall follow the standard procedure in the density matrix Liouville–von Neumann equation, in which we take into account its entire multipole component that is accessible to the D_1 configuration [14]. This approach is favourable as the selective addressing of higher rank atomic polarization multipole moments is possible, as has been shown in [15]. Furthermore, it is used to study the dependence of forward-scattering signals on the multipoles of various ranks of the density matrix [16].

Our paper is organized as follows. Section 2 presents the general description of the atomic scheme for the three-colour excitation. In Sect. 3, the tri-mode density matrix equations are derived. In addition, this section comprises a detailed description of the density matrix multipoles, the system Hamiltonian as well as the radiational and collisional contributions of the relaxation operator. In Sect. 4 we present the explicit probe's coherence to the first- and third-order in the probe field and compare them with the numerical results. The density matrix equations that have been obtained for the scheme presented in Sect. 2 are employed in Sect. 5 to describe the quantum switching effect and the three-colour EIT effect. The influence of collisional relaxation and dephasing rates, as well as the field strength dependence are analysed further in this section. In Sect. 6 we present the steady state propagation under the three-photon resonance condition revealing the main features associated with the three-colour excitation process. In Sect. 7 we employ the electromagnetically induced emission effect to generate slow-soliton trains. Finally, Sect. 8 is devoted to the concluding remarks.

2. The atomic system description

The scheme that is addressed in the paper is a combination of Λ and V configurations as shown in Fig. 1 with the appropriate dipole allowed and forbidden transitions for the D_1 line in ^{87}Rb atoms. The probe and the drive subsystem form the electromagnetically induced transparency Λ-like medium. We add the switch field in which the drive and the switch fields constitute the V-like subsystem. Let us take the hyperfine states to be denoted as: $|1\rangle = |F_1 = 1\rangle$, $|2\rangle = |F_1 = 2\rangle$,

$|3\rangle = |F_{\rm u} = 1\rangle$, and $|4\rangle = |F_{\rm u} = 2\rangle$, where l, u stands for the lower and upper hyperfine levels, respectively, and F is the total angular momentum. The probe laser with the Rabi frequency ($\Omega_{\rm p}$) is tuned to the transition $|1\rangle \leftrightarrow |3\rangle$. The drive field ($\Omega_{\rm r}$) and the switch one ($\Omega_{\rm s}$) are tuned to the transitions $|2\rangle \leftrightarrow |3\rangle$ and $|2\rangle \leftrightarrow |4\rangle$, respectively. Both of the two subsystems have their own two-photon resonance condition associated with the upper ($\Delta\omega_{\rm u}$) and lower ($\Delta\omega_{\rm l}$) hyperfine splitting.

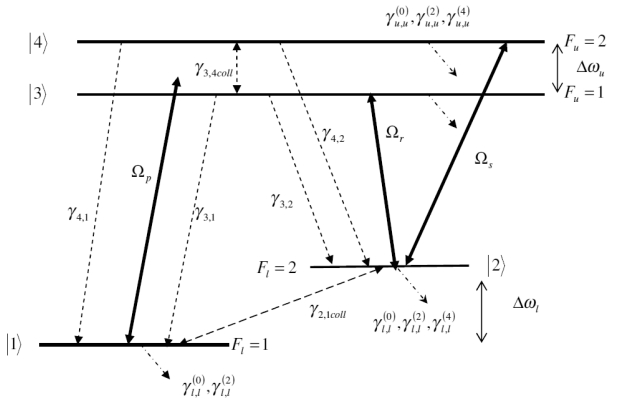

Fig. 1. The energy-level scheme for the D_1 transition in ^{87}Rb excited by the three--colour Rabi frequencies: the probe $\Omega_{\rm p}$, the drive $\Omega_{\rm r}$, and the switch $\Omega_{\rm s}$. There are given also some of the relevant decay rates both collisional and radiational. Dashed arrows indicate these rates.

We now turn to the description of decay rates. The spontaneous decay rate for the excited $P_{1/2}$ state is denoted by γ. The spontaneous decay rates of the upper hf states $\gamma_{\rm u,l}$ are related to γ by the branching ratio and we will not assume that they are equal. To account for collisional relaxation we briefly mention the most relevant collisional rates which are in turn. The collisional coherence rates between upper and lower levels are represented by $\gamma^{(k)}_{\rm l,u}$ with $k = 1, 2, 3$. In particular, the dephasing rate for the lower hf states is represented by $\gamma_{\rm l,l} = \gamma^{(2)}_{1,2}$. Also, $\gamma^{(0)}_{\rm l,l}$ and $\gamma^{(0)}_{\rm u,u}$ specifies the collisional monopole relaxation rates for the lower and upper hf states, respectively. We shall take $\gamma^{(0)}_{\rm l,l} = 10^{-8}\gamma$ and $\gamma^{(0)}_{\rm u,u} = \gamma^{(k)}_{\rm l,u} = \gamma_{\rm l,u}$ until otherwise stated. These collisional relaxations are fully detailed in the next section.

3. Tri-mode density matrix equations

The spatio-temporal propagation of the radiation fields are described by the coupled equations, the reduced Maxwell field equations for the three radiation fields and the Liouville–von Neumann equation for the density matrix of the dressed atom. Thus, let us begin by describing the total Hamiltonian of the dressed atom. It comprises of three parts as

$$H = H_{\rm s} + H_{\rm b} + H_{\rm sb}. \tag{1}$$

These terms are in order given as follows:

— the system Hamiltonian $H_{\rm s}$ describing the interaction of the atom with the multi-mode field,

— the bath Hamiltonian $H_{\rm b}$ devoting to the thermal and radiation field,

— and the system–bath Hamiltonian, $H_{\rm sb}$, which describes the atom–bath mutual interaction.

Following to that, we shall focus our attention on the system Hamiltonian. For discussions concerning $H_{\rm b}$, $H_{\rm sb}$, and how the density matrix is reduced by the elimination of the bath degrees of freedom we refer to the papers [17, 18]. Further, the system Hamiltonian can be decomposed as

$$H_{\rm s} = H_{\rm A} + H_{\rm L} + V, \tag{2}$$

where $H_{\rm A}$, $H_{\rm L}$, and V are the free atomic Hamiltonian, the free multi-mode laser Hamiltonian, and atom multi-mode laser coupling operator.

In the dipole approximation the atom–field coupling reads

$$V = -\boldsymbol{\mu} \cdot \boldsymbol{E}, \tag{3}$$

where $\boldsymbol{\mu}$ is the dipole moment operator and $\boldsymbol{E}$ stands for the polychromatic electromagnetic field

$$\boldsymbol{E} = {\rm i} \sum_{j\in({\rm p,r,s})} \frac{E_j}{2} [a_j(\boldsymbol{k}_j, z_j)\boldsymbol{\varepsilon}_j \exp({\rm i}\boldsymbol{k}_j \cdot \boldsymbol{z}_j) - a_j^+(\boldsymbol{k}_j, z_j)\boldsymbol{\varepsilon}_j^* \exp(-{\rm i}\boldsymbol{k}_j \cdot \boldsymbol{z}_j)], \tag{4}$$

where $\boldsymbol{k}_j$, $\boldsymbol{\varepsilon}_j$ and a_j $\left(a_j^+\right)$ stand for the wave vector, polarization, and the annihilation (creation) operator for the j mode of the probe (p), drive (r), and the switch (s) fields. The normalization amplitudes for the mode k_j are represented by E_j. The atomic dipole operator is represented by its lowering $\boldsymbol{d}_j$ and rising parts $\boldsymbol{d}_j^+$ and summed over the available dipole allowed hyperfine transitions

$$\boldsymbol{\mu} = \sum_{j\in({\rm p,r,s})} \boldsymbol{d}_j + \boldsymbol{d}_j^+. \tag{5}$$

The Liouville–von Neumann equation for the reduced density matrix $\rho_{\rm s}$ according to the Liouville space approach to the separable density matrix [19] is given as

$$-{\rm i}\partial_t \rho_{\rm s}(t) = (\hat{H}_{\rm s} - {\rm i}\,\hat{\Phi})\rho_{\rm s}(t), \tag{6}$$

where $\hat{H}_{\rm s}$ and $\hat{\Phi}$ stand for the system Hamiltonian and the relaxation superoperators. The superoperator is an operator acting on another operator in the product space. It is defined by the commutation relation

$$\hat{H}_{\rm s} A = -[H_{\rm s}, A]. \tag{7}$$

It is convenient to construct the Liouville space minimal basis using the irreducible set of the hyperfine states as

$$e_{ik}(Fm) = \sum_{m_i m_k} (-1)^{F_i - m_i} C\left(F_k F_i F; m_k \overline{m}_i m\right) \left|F_k m_k n_j n_j'\right\rangle \left\langle F_i m_i n_j n_j'\right|, \tag{8}$$

where F stands for the total angular momentum with the values such that $|F_i - F_k| \leq F \leq F_i + F_k$ and m is its projection. The indices i and k run over all the labels of the hf states as depicted in Fig. 1. The field-dressed ket $|F_i m_i n_j n'_j\rangle = |F_i m_i\rangle|n_j n'_j\rangle$ describes the hf state with angular momentum F_i and projection m_i depending upon the photon number n_j (n'_j) of the incident (scattered) radiation for the j mode ($k_j \lambda_j$). The Fock state with photon number n_j, i.e., $|n_j\rangle$, is represented by the product $|n_\mathrm{p}\rangle|n_\mathrm{r}\rangle|n_\mathrm{s}\rangle$. We shall suppress the dependence of basic set on the scattered radiated photons since the photon numbers n_j are large. The symbol $C(F_k F_i F; m_k \overline{m}_i m)$ stands for the Clebsch–Gordan coefficient and $\overline{m}_i = -m_i$. The operators $e_\alpha = e_{ik}$ form an orthogonal set in the Hilbert space with trace metrics as

$$(e_\alpha, e_\beta) = \mathrm{Tr}\{e_\alpha^+ e_\beta\}. \tag{9}$$

In terms of the minimal basis $\{e_\alpha\}$, the reduced density matrix is represented by the components ρ_α, in accordance with

$$\rho_\mathrm{s} = \sum_{\alpha,F,m} \rho_\alpha^{(Fm)} e_\alpha(Fm). \tag{10}$$

In the present paper, we assume that the light is linearly polarized, and in the case of polychromatic field, the polarizations are parallel. For such linear polarization, the reduced density matrix is composed of 28 components. Specifically, the first four components are related to the hf states populations $n_1, \ldots, n_4$ according to the relations

$$n_1 = \sqrt{3}\rho_1, \quad n_2 = \sqrt{5}\rho_2, \quad n_3 = \sqrt{3}\rho_3 \quad \text{and} \quad n_4 = \sqrt{5}\rho_4, \tag{11}$$

where ρ_α, $\alpha = 1, \ldots, 4$ are tensors of the 0-th rank. Next, we have eight complex components, optical coherences, of the first rank that connect the dipole allowed transitions. These are denoted by $\rho_{\mathrm{l,u}}^{(1)}$ and their adjoint, where l = (1,2) and u = (3,4) labels the lower and upper hf states, respectively. Furthermore, we have eight components of the second-rank tensors. They are $\{\rho_{1,2}^{(2)}, \rho_{2,1}^{(2)}\}$, $\{\rho_{3,4}^{(2)}, \rho_{4,3}^{(2)}\}$, and $\{\rho_{1,1}^{(2)}, \rho_{2,2}^{(2)}, \rho_{3,3}^{(2)}, \rho_{4,4}^{(2)}\}$. The first (second) couple represents the Raman coherence between the lower (upper) hf states. The last couple represents the alignment of the four hf states. In addition, there are six components of the third rank such as $\{\rho_{2,4}^{(3)}, \rho_{2,3}^{(3)}, \rho_{1,4}^{(3)}\}$, and their adjoint. Finally, we have two components of the fourth rank as $\{\rho_{2,2}^{(4)}, \rho_{4,4}^{(4)}\}$.

We now return to the matrix elements of the super-Hamiltonian operators $\hat{H}_\mathrm{A} + \hat{H}_\mathrm{L}$. It is calculated through the relations

$$\left(\hat{H}_\mathrm{A} + \hat{H}_\mathrm{L}\right) e_{1,3} = (\omega_\mathrm{p} - \omega_{3,1})\, e_{1,3}, \quad \left(\hat{H}_\mathrm{A} + \hat{H}_\mathrm{L}\right) e_{1,4} = (\omega_\mathrm{p} - \omega_{4,1})\, e_{1,4},$$

$$\left(\hat{H}_\mathrm{A} + \hat{H}_\mathrm{L}\right) e_{2,3} = (\omega_\mathrm{r} - \omega_{3,2})\, e_{2,3}, \quad \left(\hat{H}_\mathrm{A} + \hat{H}_\mathrm{L}\right) e_{2,4} = (\omega_\mathrm{s} - \omega_{4,2})\, e_{2,4},$$

$$\left(\hat{H}_\mathrm{A} + \hat{H}_\mathrm{L}\right) e_{1,2} = (\omega_\mathrm{p,r} - \omega_{2,1})\, e_{1,2}, \quad \left(\hat{H}_\mathrm{A} + \hat{H}_\mathrm{L}\right) e_{3,4} = (\omega_\mathrm{s,r} - \omega_{4,3})\, e_{3,4}. \tag{12}$$

The detuning of the fields from their appropriate transition are then defined as

$$\delta_{\rm p} = \omega_{\rm p} - \omega_{3,1}, \quad \delta_{\rm r} = \omega_{\rm r} - \omega_{3,2} \quad \text{and} \quad \delta_{\rm s} = \omega_{\rm s} - \omega_{4,2}, \tag{13}$$

where $\omega_{i,j} = \omega_i - \omega_j$.

Beside the rotating wave approximation, we shall make use of the frequency matching condition between the drive and probe field frequencies to eliminate the lower Raman frequency oscillation and to obtain the EIT medium for the lower lambda system, i.e.

$$\omega_{2,1} = \omega_{\rm p,r}. \tag{14}$$

In addition, we adopt a frequency matching condition between the upper states hf splitting $\Delta\omega_{\rm u}$ and the field's frequency difference $\omega_{\rm s,r}$ as

$$\omega_{4,3} = \omega_{\rm s,r}. \tag{15}$$

Therefore, we obtain the V-type EIT feature between drive and switching fields.

It is suitable to express the tri-mode coupling Hamiltonian matrix associated with the absorption in terms of the minimal basis $\{e_\alpha\}$ as

$$\hat{V}^- = \hat{V}_{\rm p}^- + \hat{V}_{\rm r}^- + \hat{V}_{\rm s}^-, \tag{16}$$

where $\hat{V}_{\rm p}^-$, $\hat{V}_{\rm r}^-$ and $\hat{V}_{\rm s}^-$ stand for the absorption matrix elements for the probe, drive, and switching fields, respectively, and they are given by

$$\hat{V}_{\rm p}^- = {\rm i}v_{\rm p}\left(e_{1,3}^{(1)} - \sqrt{5}e_{1,4}^{(1)}\right), \tag{17}$$

$$\hat{V}_{\rm r}^- = {\rm i}\sqrt{5}v_{\rm r}e_{2,3}^{(1)}, \tag{18}$$

$$\hat{V}_{\rm s}^- = -{\rm i}\sqrt{5}v_{\rm s}e_{2,4}^{(1)}, \tag{19}$$

where v_j, $j \in ({\rm p}, {\rm r}, {\rm s})$ are the atom–field coupling parameters depending on the corresponding transition dipole matrix elements.

Finally, we can obtain the coupling Hamiltonian matrix element through

$$\hat{V}_{\alpha\beta} = \left(e_\alpha, \hat{V}e_\beta\right). \tag{20}$$

What remains are the matrix elements corresponding to the relaxation operator both radiational and collisional. For our present study, in which the hf structure of the D_1 line is taken into account, we adopt the forms as adopted by Dangel and Holzner [20]. However, instead of the diffusion relaxation rate introduced by them we have utilized kinetic equations to present the monopole relaxation rate $\gamma_{\rm l,l}^{(0)}$ that tends to produce the thermal equilibrium. The ground state collisional dephasing rate has been recently reported in EIT experiments with condensates [21]. The atomic coherence collisional relaxation rates are represented by $\gamma_{\rm l,u}^{(1)}$. The quadrupole relaxation moments are represented by $\gamma_{1,2}^{(2)}, \gamma_{1,1}^{(2)}, \gamma_{2,2}^{(2)}, \gamma_{3,3}^{(2)}, \gamma_{4,4}^{(2)}$, and $\gamma_{3,4}^{(2)}$. The third-rank relaxation moments are represented by $\gamma_{\rm l,u}^{(3)}$. The hexadecapole relaxation moments for the upper (lower) hf levels are represented by $\gamma_{4,4}^{(4)}$ and $\gamma_{2,2}^{(4)}$, respectively. Those components of the collisional relaxation rates are

presented phenomenologically. Thus, one can add other collisional contributions such as line shifts.

Finally, the Liouville–von Neumann equation for the reduced density matrix ρ_{s} is listed in Eqs. (22), where the atom–field couplings are assumed to be related to the corresponding Rabi frequencies by the relation

$$v_i = \Omega_i/\sqrt{8}, \quad i = (\mathrm{p}, \mathrm{r}, \mathrm{s}). \tag{21}$$

Here are the tri-mode density matrix equations

$$\partial_t \rho_1 = -\gamma_{\mathrm{l,l}}^{(0)} \rho_1 - \sqrt{\frac{3}{5}} \gamma_{\mathrm{l,l}}^{(0)} \rho_2 - \frac{v_{\mathrm{p}} \rho_{1,3}^{(1)}}{\sqrt{3}} + \sqrt{\frac{5}{3}} v_{\mathrm{p}} \rho_{1,4}^{(1)} - \frac{v_{\mathrm{p}}^* \rho_{3,1}^{(1)}}{\sqrt{3}} + \sqrt{\frac{5}{3}} v_{\mathrm{p}}^* \rho_{4,1}^{(1)},$$

$$\partial_t \rho_2 = -\sqrt{\frac{3}{5}} \gamma_{\mathrm{l,l}}^{(0)} \rho_1 - \frac{3}{5} \gamma_{\mathrm{l,l}}^{(0)} \rho_2 - v_{\mathrm{r}} \rho_{2,3}^{(1)} + v_{\mathrm{s}} \rho_{2,4}^{(1)} - v_{\mathrm{r}}^* \rho_{3,2}^{(1)} + v_{\mathrm{s}}^* \rho_{4,2}^{(1)},$$

$$\partial_t \rho_3 = -\gamma_{\mathrm{u,u}}^{(0)} \rho_3 - \sqrt{\frac{3}{5}} \gamma_{\mathrm{u,u}}^{(0)} \rho_4 + \frac{v_{\mathrm{p}} \rho_{1,3}^{(1)}}{\sqrt{3}} + \sqrt{\frac{5}{3}} v_{\mathrm{r}} \rho_{2,3}^{(1)} + \frac{v_{\mathrm{p}}^* \rho_{3,1}^{(1)}}{\sqrt{3}} + \sqrt{\frac{5}{3}} v_{\mathrm{r}}^* \rho_{3,2}^{(1)},$$

$$\partial_t \rho_4 = -\sqrt{\frac{3}{5}} \gamma_{\mathrm{u,u}}^{(0)} \rho_3 - \frac{3}{5} \gamma_{\mathrm{u,u}}^{(0)} \rho_4 - v_{\mathrm{p}} \rho_{1,4}^{(1)} - v_{\mathrm{s}} \rho_{2,4}^{(1)} - v_{\mathrm{p}}^* \rho_{4,1}^{(1)} - v_{\mathrm{s}}^* \rho_{4,2}^{(1)},$$

$$\partial_t \rho_{3,1}^{(1)} = \frac{v_{\mathrm{p}} \rho_1}{\sqrt{3}} - \frac{v_{\mathrm{p}} \rho_3}{\sqrt{3}} - \frac{v_{\mathrm{p}} \rho_{1,1}^{(2)}}{\sqrt{6}} + \frac{v_{\mathrm{p}} \rho_{3,3}^{(2)}}{\sqrt{6}} - \sqrt{\frac{3}{2}} v_{\mathrm{p}} \rho_{3,4}^{(2)} - \rho_{3,1}^{(1)} \tilde{\Gamma}_{3,1}^{(1)} + \sqrt{\frac{3}{2}} v_{\mathrm{r}} \rho_{2,1}^{(2)},$$

$$\partial_t \rho_{4,1}^{(1)} = -\sqrt{\frac{5}{3}} v_{\mathrm{p}} \rho_1 + v_{\mathrm{p}} \rho_4 - \frac{v_{\mathrm{p}} \rho_{1,1}^{(2)}}{\sqrt{30}} + \sqrt{\frac{3}{10}} v_{\mathrm{p}} \rho_{4,3}^{(2)} + \sqrt{\frac{7}{10}} v_{\mathrm{p}} \rho_{4,4}^{(2)}$$
$$- \rho_{4,1}^{(1)} \tilde{\Gamma}_{4,1}^{(1)} + \sqrt{\frac{3}{10}} v_{\mathrm{s}} \rho_{2,1}^{(2)},$$

$$\partial_t \rho_{3,2}^{(1)} = v_{\mathrm{r}} \rho_2 - \sqrt{\frac{5}{3}} v_{\mathrm{r}} \rho_3 + \sqrt{\frac{3}{10}} v_{\mathrm{p}} \rho_{1,2}^{(2)} + \sqrt{\frac{7}{10}} v_{\mathrm{r}} \rho_{2,2}^{(2)} - \frac{v_{\mathrm{r}} \rho_{3,3}^{(2)}}{\sqrt{30}}$$
$$+ \sqrt{\frac{3}{10}} v_{\mathrm{s}} \rho_{3,4}^{(2)} - \rho_{3,2}^{(1)} \tilde{\Gamma}_{3,2}^{(1)},$$

$$\partial_t \rho_{4,2}^{(1)} = -v_{\mathrm{s}} \rho_2 + v_{\mathrm{s}} \rho_4 + \sqrt{\frac{3}{10}} v_{\mathrm{p}} \rho_{1,2}^{(2)} + \sqrt{\frac{7}{10}} v_{\mathrm{s}} \rho_{2,2}^{(2)} - \sqrt{\frac{3}{10}} v_{\mathrm{r}} \rho_{4,3}^{(2)}$$
$$- \sqrt{\frac{7}{10}} v_{\mathrm{s}} \rho_{4,4}^{(2)} - \tilde{\Gamma}_{4,2}^{(1)} \rho_{4,2}^{(1)},$$

$$\partial_t \rho_{1,1}^{(2)} = -\gamma_{1,1}^{(2)} \rho_{1,1}^{(2)} + \frac{v_{\mathrm{p}} \rho_{1,3}^{(1)}}{\sqrt{6}} + \frac{v_{\mathrm{p}} \rho_{1,4}^{(1)}}{\sqrt{30}} - \frac{3 v_{\mathrm{p}} \rho_{1,4}^{(3)}}{\sqrt{5}} + \frac{v_{\mathrm{p}}^* \rho_{3,1}^{(1)}}{\sqrt{6}} + \frac{v_{\mathrm{p}}^* \rho_{4,1}^{(1)}}{\sqrt{30}} - \frac{3 v_{\mathrm{p}}^* \rho_{4,1}^{(3)}}{\sqrt{5}},$$

$$\partial_t \rho_{2,2}^{(2)} = -\gamma_{2,2}^{(2)} \rho_{2,2}^{(2)} - \sqrt{\frac{7}{10}} v_{\mathrm{r}} \rho_{2,3}^{(1)} + \sqrt{\frac{3}{35}} v_{\mathrm{r}} \rho_{2,3}^{(3)} - \sqrt{\frac{7}{10}} v_{\mathrm{s}} \rho_{2,4}^{(1)}$$
$$- 3\sqrt{\frac{2}{35}} v_{\mathrm{s}} \rho_{2,4}^{(3)} - \sqrt{\frac{7}{10}} v_{\mathrm{r}}^* \rho_{3,2}^{(1)} + \sqrt{\frac{3}{35}} v_{\mathrm{r}}^* \rho_{3,2}^{(3)} - 3\sqrt{\frac{2}{35}} v_{\mathrm{s}}^* \rho_{4,2}^{(3)} - \sqrt{\frac{7}{10}} v_{\mathrm{s}}^* \rho_{4,2}^{(1)},$$

$$\partial_t \rho_{3,3}^{(2)} = -\frac{v_{\mathrm{p}} \rho_{1,3}^{(1)}}{\sqrt{6}} + \frac{v_{\mathrm{r}} \rho_{2,3}^{(1)}}{\sqrt{30}} - \frac{3 v_{\mathrm{r}} \rho_{2,3}^{(3)}}{\sqrt{5}} - \frac{v_{\mathrm{p}}^* \rho_{3,1}^{(1)}}{\sqrt{6}} + \frac{v_{\mathrm{r}}^* \rho_{3,2}^{(1)}}{\sqrt{30}} - \frac{3 v_{\mathrm{r}}^* \rho_{3,2}^{(3)}}{\sqrt{5}} - \gamma_{3,3}^{(2)} \rho_{3,3}^{(2)},$$

$$\partial_t\rho_{4,4}^{(2)} = -\sqrt{\frac{7}{10}}v_{\rm p}\rho_{1,4}^{(1)} + \sqrt{\frac{3}{35}}v_{\rm p}\rho_{1,4}^{(3)} + \sqrt{\frac{7}{10}}v_{\rm s}\rho_{2,4}^{(1)} + 3\sqrt{\frac{2}{35}}v_{\rm s}\rho_{2,4}^{(3)} - \sqrt{\frac{7}{10}}v_{\rm p}^*\rho_{4,1}^{(1)}$$
$$+\sqrt{\frac{3}{35}}v_{\rm p}^*\rho_{4,1}^{(3)} + 3\sqrt{\frac{2}{35}}v_{\rm s}^*\rho_{4,2}^{(3)} - \gamma_{4,4}^{(2)}\rho_{4,4}^{(2)} + \sqrt{\frac{7}{10}}v_{\rm s}^*\rho_{4,2}^{(1)},$$
$$\partial_t\rho_{2,1}^{(2)} = -\sqrt{\frac{3}{10}}v_{\rm p}\rho_{2,3}^{(1)} - \frac{v_{\rm p}\rho_{2,3}^{(3)}}{\sqrt{5}} - \sqrt{\frac{3}{10}}v_{\rm p}\rho_{2,4}^{(1)} + \sqrt{\frac{6}{5}}v_{\rm p}\rho_{2,4}^{(3)} - \sqrt{\frac{3}{2}}v_{\rm r}^*\rho_{3,1}^{(1)}$$
$$-\sqrt{\frac{3}{10}}v_{\rm s}^*\rho_{4,1}^{(1)} - \frac{v_{\rm s}^*\rho_{4,1}^{(3)}}{\sqrt{5}} - \tilde{\Gamma}_{2,1}^{(2)}\rho_{2,1}^{(2)},$$
$$\partial_t\rho_{4,3}^{(2)} = \sqrt{\frac{3}{2}}v_{\rm p}\rho_{1,3}^{(1)} - \sqrt{\frac{3}{10}}v_{\rm s}\rho_{2,3}^{(1)} - \frac{v_{\rm s}\rho_{2,3}^{(3)}}{\sqrt{5}} - \sqrt{\frac{3}{10}}v_{\rm p}^*\rho_{4,1}^{(1)} - \frac{v_{\rm p}^*\rho_{4,1}^{(3)}}{\sqrt{5}}$$
$$-\sqrt{\frac{6}{5}}v_{\rm r}^*\rho_{4,2}^{(3)} - \rho_{4,3}^{(2)}\tilde{\Gamma}_{4,3}^{(2)} + \sqrt{\frac{3}{10}}v_{\rm r}^*\rho_{4,2}^{(1)},$$
$$\partial_t\rho_{4,2}^{(3)} = -\sqrt{\frac{6}{5}}v_{\rm p}\rho_{1,2}^{(2)} + 3\sqrt{\frac{2}{35}}v_{\rm s}\rho_{2,2}^{(2)} + \sqrt{\frac{2}{7}}v_{\rm s}\rho_{2,2}^{(4)} + \sqrt{\frac{6}{5}}v_{\rm r}\rho_{4,3}^{(2)} - 3\sqrt{\frac{2}{35}}v_{\rm s}\rho_{4,4}^{(2)}$$
$$-\sqrt{\frac{2}{7}}v_{\rm s}\rho_{4,4}^{(4)} - \rho_{4,2}^{(3)}\tilde{\Gamma}_{4,2}^{(3)},$$
$$\partial_t\rho_{3,2}^{(3)} = \frac{v_{\rm p}\rho_{1,2}^{(2)}}{\sqrt{5}} - \sqrt{\frac{3}{35}}v_{\rm r}\rho_{2,2}^{(2)} + 2\sqrt{\frac{3}{7}}v_{\rm r}\rho_{2,2}^{(4)} + \frac{3v_{\rm r}\rho_{3,3}^{(2)}}{\sqrt{5}} + \frac{v_{\rm s}\rho_{3,4}^{(2)}}{\sqrt{5}} - \rho_{3,2}^{(3)}\tilde{\Gamma}_{3,2}^{(3)},$$
$$\partial_t\rho_{4,1}^{(3)} = \frac{3v_{\rm p}\rho_{1,1}^{(2)}}{\sqrt{5}} + \frac{v_{\rm p}\rho_{4,3}^{(2)}}{\sqrt{5}} - \sqrt{\frac{3}{35}}v_{\rm p}\rho_{4,4}^{(2)} + 2\sqrt{\frac{3}{7}}v_{\rm p}\rho_{4,4}^{(4)} - \rho_{4,1}^{(3)}\tilde{\Gamma}_{4,1}^{(4)} + \frac{v_{\rm s}\rho_{2,1}^{(2)}}{\sqrt{5}},$$
$$\partial_t\rho_{2,2}^{(4)} = -\gamma_{2,2}^{(4)}\rho_{2,2}^{(4)} - 2\sqrt{\frac{3}{7}}v_{\rm r}\rho_{2,3}^{(3)} - \sqrt{\frac{2}{7}}v_{\rm s}\rho_{2,4}^{(3)} - 2\sqrt{\frac{3}{7}}v_{\rm r}^*\rho_{3,2}^{(3)} - \sqrt{\frac{2}{7}}v_{\rm s}^*\rho_{4,2}^{(3)},$$
$$\partial_t\rho_{4,4}^{(4)} = -2\sqrt{\frac{3}{7}}v_{\rm p}\rho_{1,4}^{(3)} + \sqrt{\frac{2}{7}}v_{\rm s}\rho_{2,4}^{(3)} - 2\sqrt{\frac{3}{7}}v_{\rm p}^*\rho_{4,1}^{(3)} + \sqrt{\frac{2}{7}}v_{\rm s}^*\rho_{4,2}^{(3)} - \gamma_{4,4}^{(4)}\rho_{4,4}^{(4)}, \quad (22)$$

where we have used the notations

$$\tilde{\Gamma}_{3,1}^{(1)} = \gamma_{3,1}^{(1)} + {\rm i}(\omega_{\rm p} - \omega_{3,1}), \quad \tilde{\Gamma}_{4,1}^{(1)} = \gamma_{4,1}^{(1)} + {\rm i}(\omega_{\rm p} - \omega_{4,1}),$$
$$\tilde{\Gamma}_{3,2}^{(1)} = \gamma_{3,2}^{(1)} + {\rm i}(\omega_{\rm r} - \omega_{2,3}), \quad \tilde{\Gamma}_{4,2}^{(1)} = \gamma_{4,2}^{(1)} + {\rm i}(\omega_{\rm s} - \omega_{2,4}),$$
$$\tilde{\Gamma}_{2,1}^{(2)} = \gamma_{2,1}^{(2)} - {\rm i}(\omega_{\rm p} - \omega_{\rm r}) + {\rm i}\omega_{2,1}, \quad \tilde{\Gamma}_{4,3}^{(2)} = \gamma_{4,3}^{(2)} - {\rm i}(\omega_{\rm r} - \omega_{\rm s}) + {\rm i}\omega_{4,3},$$
$$\tilde{\Gamma}_{4,2}^{(3)} = \gamma_{4,2}^{(3)} + {\rm i}(\omega_{\rm s} - \omega_{4,2}), \quad \tilde{\Gamma}_{3,2}^{(3)} = \gamma_{3,2}^{(3)} + {\rm i}(\omega_{\rm r} - \omega_{3,2}),$$
$$\tilde{\Gamma}_{4,1}^{(3)} = \gamma_{4,1}^{(3)} + {\rm i}(\omega_{\rm p} - \omega_{4,1}). \quad (23)$$

Accordingly, the reduced Maxwell–Bloch equations for the radiation fields stand now

$$\partial_z v_j = \alpha_j' {\rm Tr}\{\mu_j\rho\}, \quad j = ({\rm p}, {\rm r}, {\rm s}), \quad (24)$$

where α_j' are the propagation constants. Let us suppose that these propagation

constants are related to the absorption coefficients α_j as

$$\alpha'_j = \alpha_j \Gamma_j / 3, \tag{25}$$

and Γ_j are the coherence decay rates for the relevant optical transitions. The one-third is involved to the state that we are dealing with π polarized light. It is instructive to incorporate the propagation Eqs. (24) with the generated three--wave mixing field corresponding to the transition $|1\rangle \leftrightarrow |4\rangle$ through the governing equation as

$$\partial_z v_{\mathrm{twm}} = \alpha'_{\mathrm{twm}} \mathrm{Tr}\{\mu_{\mathrm{p}} \rho\}, \tag{26}$$

with μ_{p} in this case devoted to the probe's dipole moment corresponding to the transition $|1\rangle \leftrightarrow |4\rangle$ only. Strictly speaking, we have specified the three-wave mixing field as generated by the off-resonant coherence $\rho_{1,4}$. Its impact on the other fields has not been implemented explicitly. Thus, the density matrix equations are only functions of the three applied fields, the probe, drive, and switching field. For numerical simulation, we shall ignore the difference between these α_j's and equate them to the absorption coefficient of the probe in the absence of the other fields. Additionally, we use the spontaneous decay rate γ instead of Γ_j in Eq. (25) as for we do not have strong pressure broadening.

Finally, the tri-mode density matrix equations presented in Eqs. (22), are coupled to the radiation fields through the reduced Maxwell field equations in which the average dipole moments are given by

$$d_{\mathrm{p}} = \frac{\mathrm{i}}{\sqrt{6}} \left(\rho_{3,1} - \sqrt{5} \rho_{4,1} \right), \tag{27}$$

$$d_{\mathrm{r}} = \mathrm{i} \rho_{3,2}, \tag{28}$$

$$d_{\mathrm{s}} = -\mathrm{i} \rho_{4,2}. \tag{29}$$

4. The explicit probe's first- and second-order susceptibility

The probe's coherence to the first order in the probe's field and higher orders in the drive and switching fields is given by

$$\begin{aligned} \frac{\mathrm{i}\rho_{2,1}}{\sqrt{6}} = \mathcal{L}(v_{\mathrm{r}}^2) \Bigg\{ & \left[-\frac{\mathrm{i}}{3\xi_{\mathrm{p}}} - \frac{v_{\mathrm{r}} v_{\mathrm{s}}}{\Gamma_{\mathrm{R}} \xi_{\mathrm{p}} (\xi_{\mathrm{p}} - 2\mathrm{i}\Delta\omega_{\mathrm{u}})} \right] \sqrt{2} v_{\mathrm{p}} \rho_1^{(0)} \\ & + \left[\frac{v_{\mathrm{r}}^2}{\Gamma_{\mathrm{R}} \xi_{\mathrm{p}} \xi_{\mathrm{r}}} - \frac{v_{\mathrm{r}} v_{\mathrm{s}}}{\Gamma_{\mathrm{R}} \xi_{\mathrm{p}} \xi_{\mathrm{s}}} \right] \sqrt{\frac{6}{5}} v_{\mathrm{p}} \rho_2^{(0)} + \left[\frac{\mathrm{i}}{3\xi_{\mathrm{p}}} - \frac{v_{\mathrm{r}}^2}{\Gamma_{\mathrm{R}} \xi_{\mathrm{p}} \xi_{\mathrm{r}}} \right] \sqrt{2} v_{\mathrm{p}} \rho_3^{(0)} \\ & + \left[\frac{1}{\Gamma_{\mathrm{R}} \xi_{\mathrm{p}} (\xi_{\mathrm{p}} - 2\mathrm{i}\Delta\omega_{\mathrm{u}})} + \frac{1}{\Gamma_{\mathrm{R}} \xi_{\mathrm{p}} \xi_{\mathrm{s}}} \right] \sqrt{\frac{6}{5}} v_{\mathrm{p}} v_{\mathrm{r}} v_{\mathrm{s}} \rho_4^{(0)} \Bigg\} \end{aligned} \tag{30}$$

with the substitutions

$$\Big\{ \xi_{\mathrm{p}} \to \gamma + 2\Gamma_{\mathrm{coll}} + 2\mathrm{i}\delta_{\mathrm{p}}, \quad \Gamma_{\mathrm{R}} \to \delta_{\mathrm{p}} - \delta_{\mathrm{r}} - \mathrm{i}\Gamma_{1,2}, \quad \xi_{\mathrm{r}} \to \gamma + 2\Gamma_{\mathrm{coll}} - 2\mathrm{i}\delta_{\mathrm{r}},$$

$$\xi_{\mathrm{s}} \to \gamma + 2\Gamma_{\mathrm{coll}} - 2\mathrm{i}\delta_{\mathrm{s}} \Big\},$$

$$\mathcal{L}^{-1}(v_{\rm r}^2)\rightarrow\frac{3{\rm i}v_{\rm r}^2}{\Gamma_{\rm R}\xi_{\rm p}}-1,\quad \Gamma_{\rm coll}=\gamma_{\rm u,l}^{(q)}=\gamma_{\rm u,u}^{(q)},\quad q\geq 1\quad\text{and}\quad \Gamma_{1,2}=\gamma_{1,2}^{(2)}.\ (31)$$

In the previous expression for the probe's coherence, we have ignored the contribution due to $\rho_{4,1}$ since it is small, as we have chosen the probe's resonance so close to the $|1\rangle\leftrightarrow|3\rangle$ transition.

The probe's coherence $\rho_{3,1}$ can be found to the third order in the probe's field $v_{\rm p}$ and higher order in the other fields. The linear term of $\rho_{3,1}$ in the probe's field is expressed as

$$\begin{aligned}
&\Big(2\Big\{3{\rm i}[2\Delta\omega_{\rm u}+{\rm i}\xi_{\rm p}]\xi_{\rm s}[3\sqrt{5}\rho_2^{(0)}-5\sqrt{3}\rho_3^{(0)}]v_{\rm r}^2+3v_{\rm s}\xi_{\rm r}\Big[-6{\rm i}\sqrt{5}\Delta\omega_{\rm u}(\rho_2^{(0)}-\rho_4^{(0)})\\
&\quad+3\sqrt{5}\xi_{\rm p}(\rho_2^{(0)}-\rho_4^{(0)})+\xi_{\rm s}(5\sqrt{3}\rho_1^{(0)}-3\sqrt{5}\rho_4^{(0)})\Big]v_{\rm r}\\
&\quad+5\sqrt{3}\Gamma_{\rm R}[2\Delta\omega_{\rm u}+{\rm i}\xi_{\rm p}]\xi_{\rm r}\xi_{\rm s}\Big[\rho_1^{(0)}-\rho_3^{(0)}\Big]\Big\}\Gamma_{1,2}\left\{3v_{\rm r}^2-{\rm i}\Gamma_{\rm R}^*\xi_{\rm p}^*\right\}\Big)\\
&\quad\Big/\Big(5\{\xi_{\rm p}-2{\rm i}\Delta\omega_{\rm u}\}\xi_{\rm r}\xi_{\rm s}\left\{[3{\rm i}(\Gamma_{\rm R}-\Gamma_{\rm R}^*)v_{\rm r}^2+\Gamma_{\rm R}\Gamma_{\rm R}^*(\xi_{\rm p}+\xi_{\rm p}^*)]v_{\rm p}^2\right.\\
&\quad\left.+3[3v_{\rm r}^2+{\rm i}\Gamma_{\rm R}\xi_{\rm p}]\Gamma_{1,2}\left[3v_{\rm r}^2-{\rm i}\Gamma_{\rm R}^*\xi_{\rm p}^*\right]\right\}\Big),
\end{aligned}\tag{32}$$

while the cubic term is found to be

$$\begin{aligned}
&\Big(2\Big\{3\xi_{\rm s}\Big[(2\Delta\omega_{\rm u}+{\rm i}\xi_{\rm p})\left(3\sqrt{5}\rho_2^{(0)}-5\sqrt{3}\rho_3^{(0)}\right)\Gamma_{\rm R}^*(2{\rm i}\Delta\omega_{\rm u}+\xi_{\rm p}^*)\xi_{\rm r}^*\\
&\quad+\Gamma_{\rm R}\xi_{\rm r}\Big(4{\rm i}\left\{3\sqrt{5}\rho_2^{(0)}-5\sqrt{3}\rho_3^{(0)}\right\}\Delta\omega_{\rm u}^2-2\left\{3\sqrt{5}\rho_2^{(0)}-5\sqrt{3}\rho_3^{(0)}\right\}\\
&\quad\times\{\xi_{\rm p}-\xi_{\rm p}^*\}\Delta\omega_{\rm u}+{\rm i}\left\{\left[5\sqrt{3}\rho_1^{(0)}-3\sqrt{5}\rho_4^{(0)}\right]\xi_{\rm p}^*\xi_{\rm r}^*\right.\\
&\quad\left.+\xi_{\rm p}\left[\left(3\sqrt{5}\rho_2^{(0)}-5\sqrt{3}\rho_3^{(0)}\right)\xi_{\rm p}^*+\left(5\sqrt{3}\rho_1^{(0)}-3\sqrt{5}\rho_4^{(0)}\right)\xi_{\rm r}^*\right]\right\}\Big)\Big]\xi_{\rm s}^*v_{\rm r}^2\\
&\quad+3v_{\rm s}\xi_{\rm r}\xi_{\rm r}^*\Big[\Big(-6{\rm i}\sqrt{5}\Delta\omega_{\rm u}\left\{\rho_2^{(0)}-\rho_4^{(0)}\right\}+3\sqrt{5}\xi_{\rm p}\left\{\rho_2^{(0)}-\rho_4^{(0)}\right\}\\
&\quad+\xi_{\rm s}\left\{5\sqrt{3}\rho_1^{(0)}-3\sqrt{5}\rho_4^{(0)}\right\}\Big)\Gamma_{\rm R}^*(2\Delta\omega_{\rm u}-{\rm i}\xi_{\rm p}^*)\xi_{\rm s}^*\\
&\quad+\Gamma_{\rm R}(2\Delta\omega_{\rm u}+{\rm i}\xi_{\rm p})\xi_{\rm s}\Big(-6{\rm i}\sqrt{5}\Delta\omega_{\rm u}\left\{\rho_2^{(0)}-\rho_4^{(0)}\right\}\\
&\quad+3\sqrt{5}\left\{\rho_4^{(0)}-\rho_2^{(0)}\right\}\xi_p^*+\left\{3\sqrt{5}\rho_4^{(0)}-5\sqrt{3}\rho_1^{(0)}\right\}\xi_{\rm s}^*\Big)\Big]v_{\rm r}\\
&\quad+\ \Gamma_{\rm R}\xi_{\rm r}\xi_{\rm s}\left[5\sqrt{3}\rho_1^{(0)}-3\sqrt{5}\rho_4^{(0)}\right]\Gamma_{\rm R}^*\xi_{\rm p}^*[\xi_{\rm p}+\xi_{\rm p}^*]\xi_{\rm r}^*\xi_{\rm s}^*\Big\}\Big)\\
&\quad\Big/\Big(15\{2\Delta\omega_{\rm u}+{\rm i}\xi_{\rm p}\}\xi_{\rm r}\xi_{\rm s}\{2\Delta\omega_{\rm u}-{\rm i}\xi_{\rm p}^*\}\{[3{\rm i}(\Gamma_{\rm R}-\Gamma_{\rm R}^*)v_{\rm r}^2+\Gamma_{\rm R}\Gamma_{\rm R}^*(\xi_{\rm p}+\xi_{\rm p}^*)]v_{\rm p}^2\\
&\quad+3[3v_{\rm r}^2+{\rm i}\Gamma_{\rm R}\xi_{\rm p}]\Gamma_{1,2}[3v_{\rm r}^2-{\rm i}\Gamma_{\rm R}^*\xi_{\rm p}^*]\}\xi_{\rm r}^*\xi_{\rm s}^*\Big).
\end{aligned}\tag{33}$$

In Fig. 2 we present the comparison of the explicit first- and third-order probe's susceptibility as well as the numerical one for the case when the probe and switching fields are at resonance with their respective transitions. In our calculations, we shall make use of the relative units. The Rabi frequencies, the

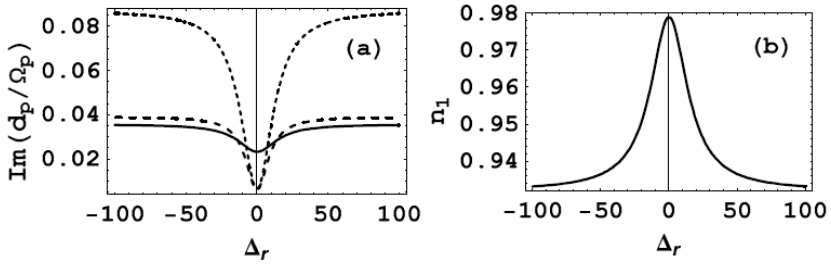

Fig. 2. The probe's absorption (part (a)) and the population (part (b)) of the first ground hf level are shown as a function of the drive field detuning. The probe and the switch fields are assumed to be in resonance with their respective transitions in this figure and hence after. The fields are weak as $\Omega_{\rm p} = 0.04,\ \Omega_{\rm r} = \Omega_{\rm s} = 0.06$. The collisional relaxation rates are taken to be as $\gamma_{\rm l,u} = 0.04$ and $\gamma_{\rm l,l} = 10^{-4}$. The continuous line is devoted to the numerical solution of the full density matrix equations. The dashed line represents the probe's absorption as calculated from Eq. (30) for the probe's coherence to the first order in the probe's field and higher orders in the drive and switching fields. The long dashed line represents the probe's absorption as calculated from the explicit third--order coherence in Eq. (32) and Eq. (33). The detuning $\Delta_{\rm r}$ is defined as $\Delta_{\rm r} = \delta_{\rm r}/\gamma_{\rm l,l}$.

detuning, the relaxation rates are measured in the units of the spontaneous decay rate γ of the excited state $P_{1/2}$. Throughout our paper, the probe and the switch fields are kept at resonance with their respective transitions until stated otherwise. We assume for the sake of comparison that the fields are weak as $\Omega_{\rm p} = 0.04$ and $\Omega_{\rm r} = \Omega_{\rm s} = 0.06$. The populations appearing in the explicit expressions for the probe's coherence are taken from the numerical solution of the density matrix at the three-photon resonance condition. It is obvious from Fig. 2a that the first--order probe's coherence is a poor approximation and better agreement is attained using the 3rd order one for off-resonance in the drive frequency. This is because in the first-order expression for the probe's coherence we have solved the density matrix equations for the lower Raman coherence $\rho^{(2)}_{1,2}$ and ignored other $\rho^{(2)}_{\alpha,\beta}$ for lower and upper hyperfine levels. As those $\rho^{(2)}_{\alpha,\beta}$ for the lower levels, other than the Raman coherence, represent losses. Thus, the third-order probe's coherence diminishes and gets closer to the numerical solution for off-resonance. A discrepancy is noted near the resonance. Unfortunately, the differences are higher than the effects which we are looking for. This needs inclusion of higher rank components, which makes our approximation lengthy and tedious. Our explicit results for the third-order susceptibility to the probe field do not show agreement with the numerical solution of the density matrix equations for two reasons. The first one is that our explicit results are only up to the second-rank tensor components. The second reason is that the populations in the explicit results for the probe's absorption do not depend on the detuning and remain constant as it is a poor assumption. However, these explicit results might be important for hot atoms as

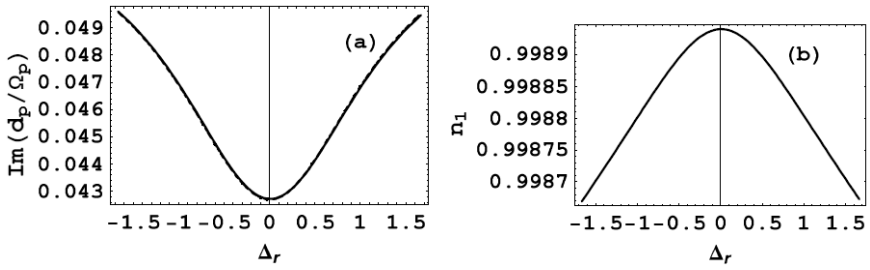

Fig. 3. The probe's absorption (part (a)) and the population (part (b)) of the first ground hf level are shown as a function of the drive field detuning. In this figure, we have assumed that the drive and switching fields are relatively stronger than the probe field as $\Omega_{\rm p} = 0.04$, $\Omega_{\rm r} = \Omega_{\rm s} = 0.6$. The collisional relaxation rates are taken to be $\gamma_{\rm l,u} = 0.4$ and $\gamma_{\rm l,l} = 0.3$. The numerical solution for the probe's absorption, the first- and third-order probe's explicit coherence gets close to each other, in contrast to the situation presented in Fig. 2. The populations in Fig. 3b merely remain in the first ground hf level.

well as the thermal equilibrium attained. So, one can find an explicit dependence of the group velocity on the relaxation rates. Furthermore, the dependence on the Doppler broadening might be included through the Cauchy principle value integral. For the present study as those for cold atoms, this explicit dependence is important to manipulate (maximize or minimize) the nonlinear dependence on the collisional decay rates. For instance, we attain agreement shown in Fig. 3 for the probe's absorption while the drive and switching fields are relatively stronger than the probe field. The collisional relaxation rates are also higher than that implemented in Fig. 2. The population depicted in Fig. 3b shows that it is mainly in the first hf ground level. So first-order as well as third-order coherence in the probe's field nearly matches the numerical results. Therefore, this approach is adequate for cold atoms as well as the atoms remaining merely at the lower hf ground level. That might explain effects like EIT but does not such as the quantum switching effect and the three-photon EIT effect because the distribution of populations amongst the detuning is nonlinear.

In fact, the essence of our theoretical treatment of the three-colour excitation of alkali-metal vapours is to show the gain experienced by the drive field while the probe and switch are attenuating. Moreover, the issue is that such amplification in cold atoms occurs because of the enhancement of higher order rank of the density matrix, which is beyond the alignment. It is worth mentioning that the explicit approach to the solution of the density matrix does not give the satisfactory result for the dependence of the absorption on the detuning or on the field strength. Therefore, our treatment for the three-colour excitation is numerical in principle.

5. The quantum switching effect and the three-colour EIT

Let us consider the situation when the applied fields are weaker than the spontaneous decay rate γ. In Fig. 4 we present the absorption of the probe, drive, and switch fields as calculated from the numerical integration of the full density matrix whose elements are listed in Eqs. (22). We represent these numerical calculations by the continuous lines in this figure. The long dashed curves in the same figure correspond to the numerical integration of a subset of the full density matrix listed in Eqs. (22). The subset contains density matrix elements up to the alignments only, i.e., we do not include third- or fourth-rank components. Therefore, the number of equations is reduced from 28 to 20. The short dashed lines are devoted to two-colour excitation in which the probe and the drive are the only relevant fields sharing a common excited state, $|3\rangle$ and having off-resonance components, i.e. $\rho_{1,4}$ and $\rho_{2,4}$ for the probe and drive fields, respectively. Furthermore, Fig. 4 shows the gain experienced by the drive field as well as the absorption of the probe and the switch field at different detuning for the drive field. It is remarkable that under the two-colour EIT based calculations the spectrum profile of the drive field does not show any enhancement. Inspection of Fig. 4 shows that the

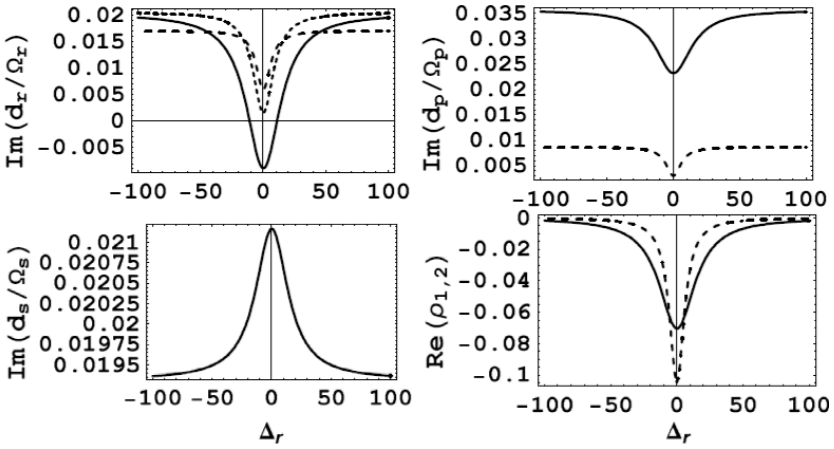

Fig. 4. The dependence of the imaginary part of the dipole moments for the drive, probe, and switch fields as well as the real part of the lower Raman coherence on the detuning of the drive field. The continuous curves are devoted to the numerical integration of the Liouville–von Neumann equations for the density matrix. The short dashed lines are devoted to two-colour excitation, which the probe and the drive are the only relevant fields sharing a common excited state, $|3\rangle$ and having off-resonance components, i.e., $\rho_{1,4}$ and $\rho_{2,4}$ for the probe and drive fields, respectively. The long dashed curves correspond to the numerical integration of the density matrix up to the alignments, i.e., we do not include third- or fourth-rank components. In this figure, we have assumed that the fields are relatively weak. $\Omega_{\rm p} = 0.04$, $\Omega_{\rm r} = \Omega_{\rm s} = 0.06$. The collisional relaxation rates are taken as $\gamma_{\rm l,u} = 0.04\gamma$ and $\gamma_{\rm l,l} = 10^{-4}\gamma$.

enhancement on the drive field spectrum is inevitably connected to the enhancement of the third- and fourth-rank components of the density matrix. Simply, the usual description in terms of the populations, the orientation and alignments is not sufficient to reveal the gain feature in the spectrum. The three-photon EIT in Fig. 4 manifests itself in the increased absorption of the probe compared with the two-photon EIT as a consequence of the quantum switching effect. Furthermore, it manifests itself in the gain experienced by the drive field at the expense of the probe as well as the switch fields. Apart from that, the real part of the Raman coherence is shown to be smaller than that of the two-photon EIT. As so, we expect a less pronounced light storage, for the three-photon EIT based experiment for weak fields. As a rule, the switch field destroys the coherent admixture of the quantum information written by the probe field and read out by the drive field. However, it creates other place for information storage, which was not noticed earlier, that is the upper Raman coherence, i.e., $\rho_{3,4}$ as shown in Fig. 5. With the help of the upper Raman coherence one can transfer the quantum information to other systems through a ladder configuration. Also, Fig. 5 displays the generated three-wave mixing coherence $\rho_{1,4}$, its dispersion as well as absorption. The three-wave mixing absorption manifests dispersion-like profile with attenuation for red drive field detuning and gain for blue detuning. Next, we examine a special case of the Raman scattering for the three-colour EIT system, which is the Rayleigh scattered light. Figure 6 shows an exposed sub-natural three-photon EIT window for the cross-section associated with the coherent (Rayleigh) scattered light. The cross-section is defined as the ratio of the square of the absolute value for the dipole moment divided by the square of the Rabi frequency. At the three-photon resonance condition, the Rayleigh scattered light by the drive is slightly increased due to the electromagnetically induced emission noted in Fig. 4. As the drive absorption vanishes, out of resonance at $\Delta_{\rm r} \approx \pm 10$, the Rayleigh scattered light is then due to the

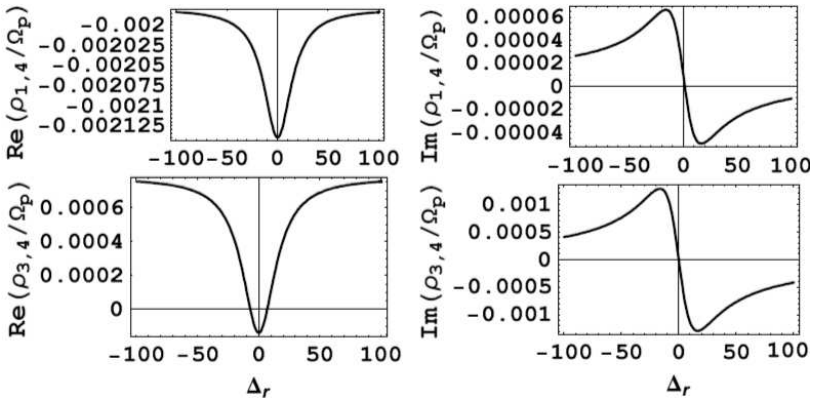

Fig. 5. The dependence of the generated three wave-mixing coherence $\rho_{1,4}$ as well as the upper Raman coherence $\rho_{3,4}$ on the detuning of the drive field. The fields are assumed to be $\Omega_{\rm p} = 0.04$, $\Omega_{\rm r} = \Omega_{\rm s} = 0.06$. The collisional relaxation rates are taken as $\gamma_{\rm l,u} = 0.04\gamma$ and $\gamma_{\rm l,l} = 10^{-4}\gamma$.

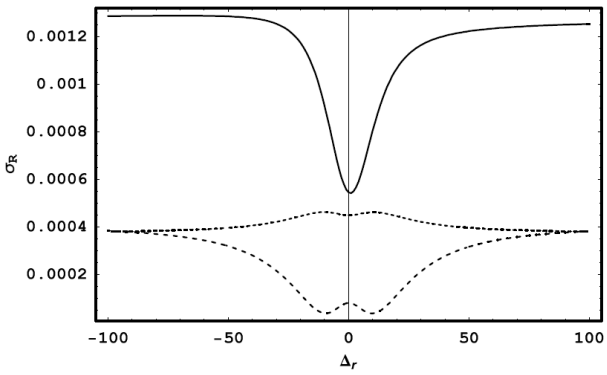

Fig. 6. The cross-section for the Rayleigh scattered light (σ_{R}) as a function of the drive field detuning. The continuous, long dashed, and dashed lines correspond to the cross--sections for the probe, drive, and switch fields, respectively. The detuning is given in terms of the lower Raman coherence $\gamma_{1,1}$. The fields as well as the collisional relaxation rates are assumed to be as in Fig. 5.

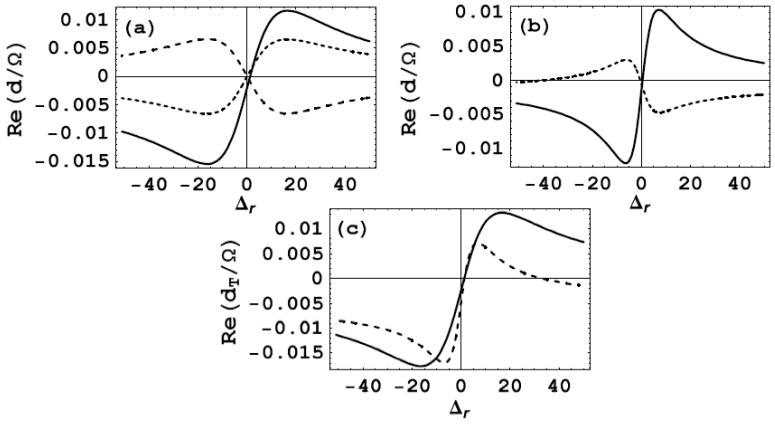

Fig. 7. In (a), given the real part of the dipole moment for probe (continuous), drive (long dashed), and switch (dashed) fields versus the detuning of the drive field. The parameter Ω denotes the relevant Rabi frequency associated to the probe (continuous), drive (long dashed), and switch (dashed) fields. In (b), given the real part of the dipole moment for probe (continuous) and drive (dashed) fields. The parameter Ω denotes the relevant Rabi frequencies associated to the probe (continuous) and drive (dashed) fields. In (c), given the real part of the total dipole moment for 3-colour EIT (continuous) and 2-colour EIT (long dashed) versus the detuning of the drive field. The parameter Ω denotes the Rabi frequency associated to the 3-colour EIT (continuous) and 2-colour EIT (long dashed) as $\Omega = \sqrt{\sum \Omega_j^2}$ where the summation is taken over the available fields.

dispersion of the drive dipole moment. Far from resonance the profile results from both the absorption and the dispersion. Such explanation may be sufficient as well as the fields are not strong and the power broadening is neglected. The real parts of the dipole moment for the probe, drive, and switch fields are depicted in Fig. 7a for three-colour EIT case. Figure 7b shows the two-colour situation for the probe and drive field. The probe's dispersion in both cases is normal and steeper in the two--colour situation. Thus, we may expect a big delay associated with the two-colour over its three-colour alternative. The drive in case (b) advances due to the anomalous dispersion, while in case (a) the drive delays. The total dipole moment for the 3-colour excitation is defined as one third of the summation of the probe, drive, and switch dipole moments. The negative value of the total dipole moment at the three-photon resonance (case (c)) as well as that at the two-photon resonance (case (b)) is a purely quantum interference effect since the static polarizability for the rubidium D_1 line is known to be positive.

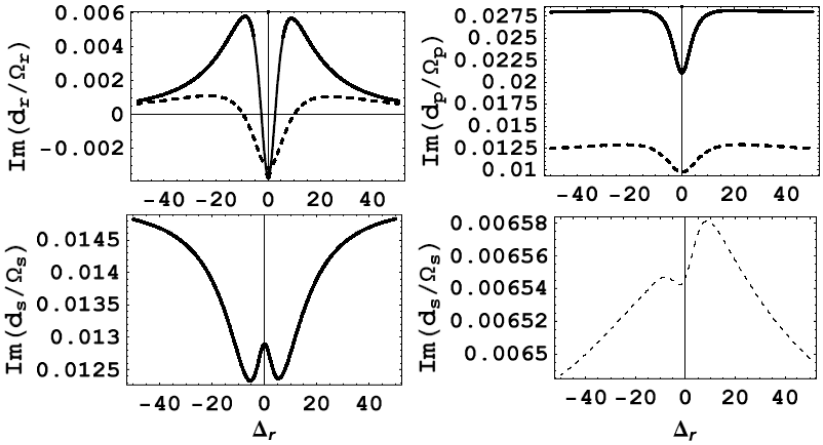

Fig. 8. The dependence of the imaginary part of the dipole moments for the drive, probe, and switch fields as a function of the drive field frequency. The continuous curves correspond to the field values $\Omega_{\rm p} = 1$ and $\Omega_{\rm r} = 1.2$, $\Omega_{\rm s} = 1.5$. The dashed lines correspond to the field values $\Omega_{\rm p} = 2$ and $\Omega_{\rm r} = 2.4$, $\Omega_{\rm s} = 3$. The collisional relaxation rates are assumed to be as $\gamma_{\rm l,l} = 0.12$ and $\gamma_{\rm l,u} = 0.3$.

So far, we have limited ourselves to the weak field cases. In Fig. 8, the situation where the fields are strong is considered. At the three-photon resonance condition, the gain in the drive field is pronounced as well as the effect of power broadening.

6. The quantum switching effect and the three-colour EIT in the course of steady state propagation

As a matter of fact, it is important to testify this prominent gain enhancement on the drive field through the course of steady state propagation of the

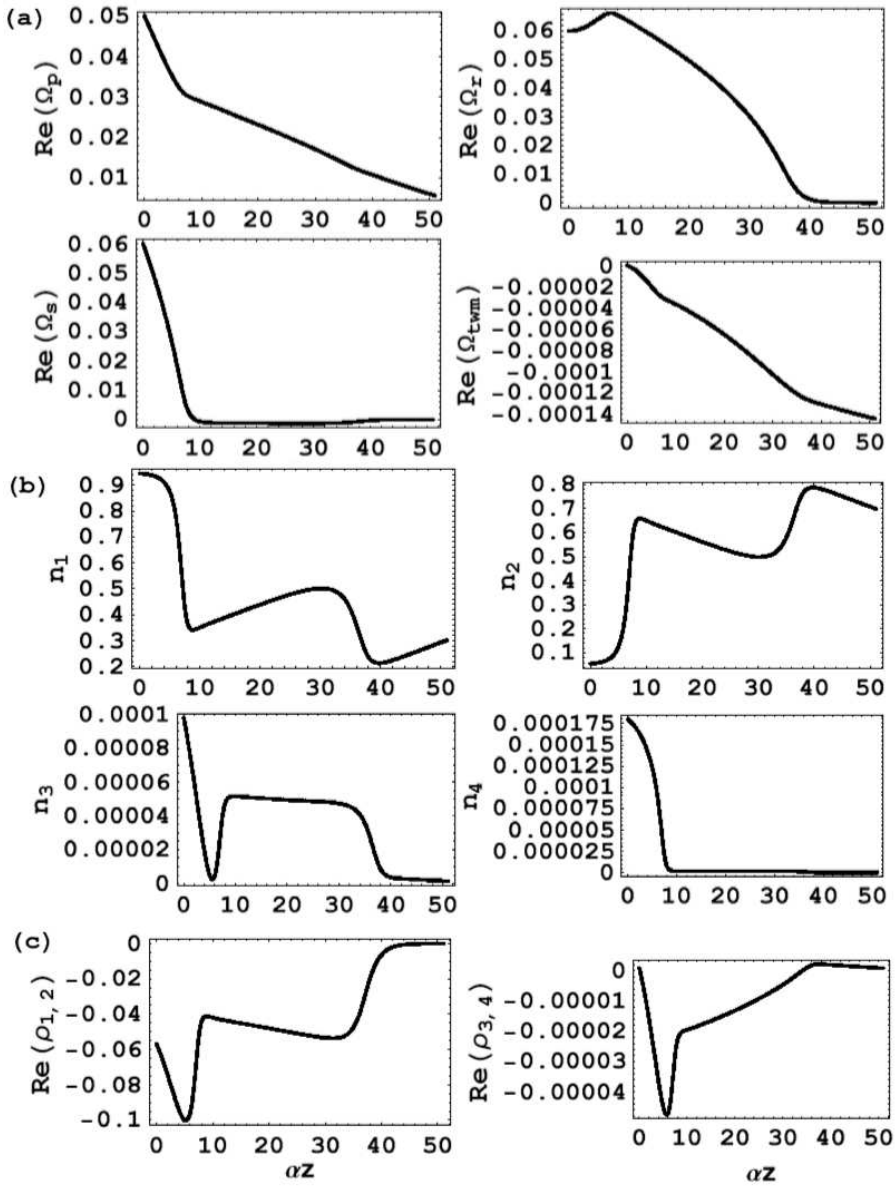

Fig. 9. (a) The figure shows the space dependence of the probe, drive, and switch fields in the course of the steady state propagation. At the boundary $z = 0$, the fields assumed to be weak as $\Omega_{\rm p} = 0.05$ and $\Omega_{\rm r} = \Omega_{\rm s} = 0.06$. The relaxation rates for this case are assumed to be $\gamma_{\rm l,u} = 0.04$, $\gamma_{\rm l,l} = 10^{-4}$ and $\gamma_{\rm l,l}^{(0)} = 10^{-5}$. We show also the generated three-wave mixing $\Omega_{\rm twm}$ field. The fields are linearly polarized and co-linearly propagating. The absorption coefficient of the probe field in the absence of the others is denoted by $\alpha_{\rm p}$. Here we have ignored the differences in α's. (b) The hyperfine level populations are shown for the case presented in part (a). (c) The space dependence of the generated lower Raman coherence as well as the upper Raman coherence is presented for the case shown in part (a).

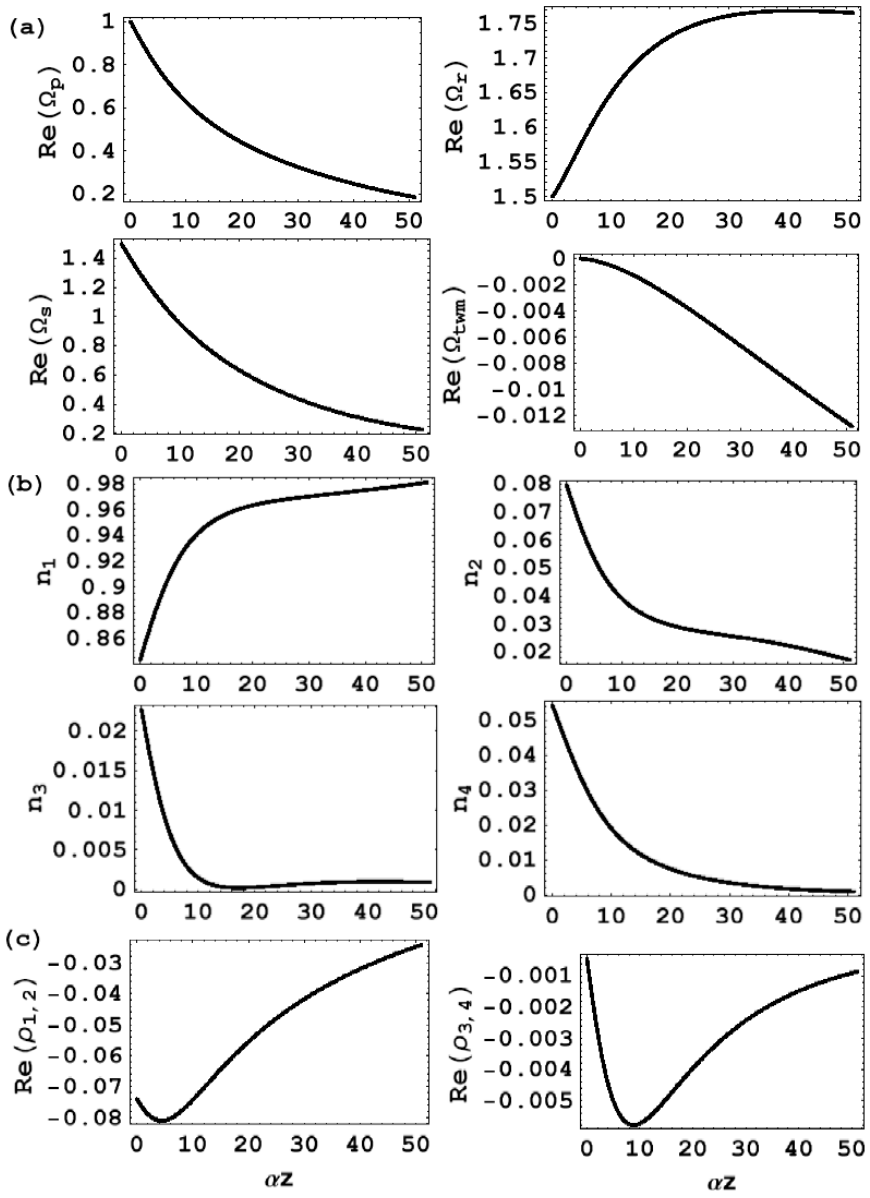

Fig. 10. (a) The figure shows the space dependence of the probe, drive, and switch fields in the course of the steady state propagation. At the boundary $z = 0$, the fields are relatively stronger than that in Fig. 9. It is assumed to be as $\Omega_{\rm p} = 1$ and $\Omega_{\rm r} = \Omega_{\rm s} = 1.5$. The relaxation rates for this case are taken as $\gamma_{\rm l,u} = 0.3$ and $\gamma_{\rm l,l} = 0.12$. There is shown also the generated three-wave mixing $\Omega_{\rm twm}$ field. (b) The hyperfine level populations are shown for the case presented in part (a). (c) The space dependence of the generated lower Raman coherence as well as the upper Raman coherence is presented for the case shown in part (a).

applied fields. Let us assume that at the boundary $z = 0$, the applied fields have weak Rabi frequencies values as $\Omega_{\rm p} = 0.05$, $\Omega_{\rm r} = 0.06$, and $\Omega_{\rm s} = 0.06$. The relaxation rates for this case are assumed to be $\gamma_{\rm l,u} = 0.04$, $\gamma_{1,2} = 10^{-4}$ and $\gamma_{\rm l,l}^{(0)} = 10^{-5}$. Figure 9a shows a slight amplification produced during the propagation of the drive field for small z as well as the attenuation in the probe and switch fields. The process is associated with *population transfer* to the second hf level in a nonlinear behaviour. For $\alpha z > 10$, the switch field is absorbed and the process is reversed, where all fields are depleted. For long distance as $\alpha z > 30$, the second level population once more rises and one can see the *switch field generation* as a consequence of the two-photon process enhancement. The generated three wave--mixing field associated with the $\rho_{1,4}$ coherence is shown to be small as depicted in Fig. 9a. The amount of information stored through the lower Raman coherence in Fig. 9c is remarkable although the fields are weak, which characterize the coherent population trapping. In Fig. 10a–c the situation of stronger applied fields is considered. The amplification on the drive as well a pronounced three-wave mixing field is attained. This time, the population of the first hf level is growing up leading to slow depletion of the probe field. Thus the amplification on the drive lasts longer in this case and in contrast with the previous case for the weak field one. The information stored in the lower as well as the upper Raman coherence gets smaller for long distances and the three-wave mixing field gets bigger. We observe also the gain experienced by the switch field for long distances on account of the depletion of the drive field.

7. Quantum optical soliton generation via electromagnetically induced emission

Let us employ the light storage effect in a hypothetical experiment as follows. The probe ($\Omega_{\rm p}$), drive ($\Omega_{\rm r}$), and switch ($\Omega_{\rm s}$) fields are tuned as presented in Fig. 1. All these fields are Gaussian pulses centred initially at $t = 0$. The probe pulse is confined through the duration time of the drive and switch fields. Furthermore, we add two delayed components in the probe channel, denoting them by $\Omega_{\rm p}^{(1)}(t - t_{\rm p}^{(1)})$ and $\Omega_{\rm p}^{(2)}(t - t_{\rm p}^{(2)})$. The delayed components are centred at the times $t_{\rm p}^{(1)}$ and $t_{\rm p}^{(2)}$, respectively. It is separated from each other with a reasonable period to prevent their overlap. Our setup for the proposed experiment is presented in Fig. 11. The numerical results at $z = 0$ for the first hf level as well as the Raman coherence is depicted in Fig. 12. Indeed, the Raman coherence explores the light storage effect in view of our previous paper [12]. Also, the electromagnetically induced emission (EIE) effect is prominent on account of increased absorption of the probe field. The light storage effect is evident in the drive field as well, as we have designated. Through the first induction period, the probe ($\Omega_{\rm p}$) and the drive ($\Omega_{\rm r}$) show good resemblance to the two-colour EIT effect [13]. It is worth mentioning that the Raman coherence does not vanish for a long time. So, one can further apply another probe pulse in the probe channel to obtain its response on the drive field

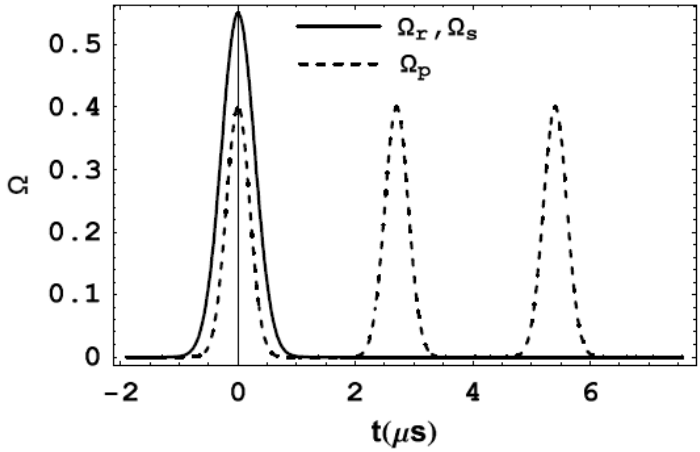

Fig. 11. The temporal behaviour of the probe, drive, and switch fields at $z = 0$. Two probe pulses added in the probe channel to check the EIE effect. These extra pulses are centred around 2.7 μs and 5.4 μs. The drive and switch pulses are chosen to be of the same shape.

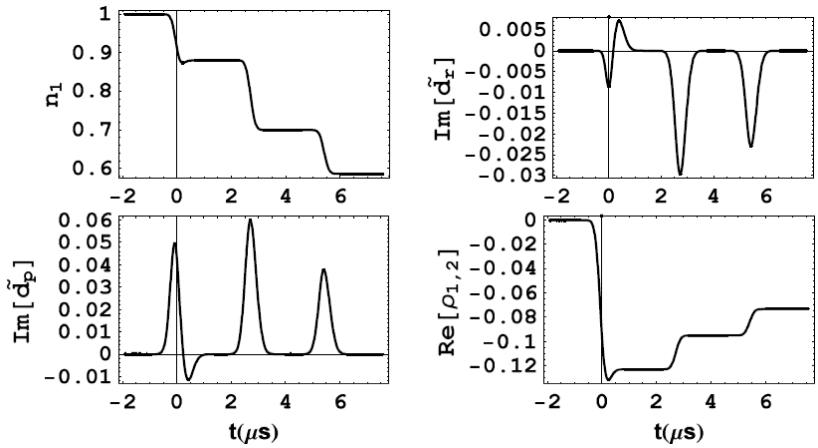

Fig. 12. The population of the first hf level, the absorption of the drive and the probe field as well as the Raman coherence at $z = 0$. The parameters for the relaxation rates and detuning are as follows: $\Delta_{\rm p} = \Delta_{\rm r} = 0$, $\Delta_{\rm s} = 0.1\Delta\omega_{\rm u}$, $\gamma_{\rm l,u} = 0.01, \gamma_{\rm l,l} = 10^{-5}$ and $\tilde{d}_j = d_j/\Omega_j(0,0)$.

revealing further the light retrieval phenomenon. It is important to notice that during switching off the pulses, we do not have any absorption. This is guaranteed by the low value of the Raman coherence dephasing rate. Thus, we have obtained a soliton train not only on the drive channel as designated but also in the probe and switch channels; this behaviour is exposed in Fig. 13. The generated wave trains in the switch channel are guaranteed by the presence of the upper Raman

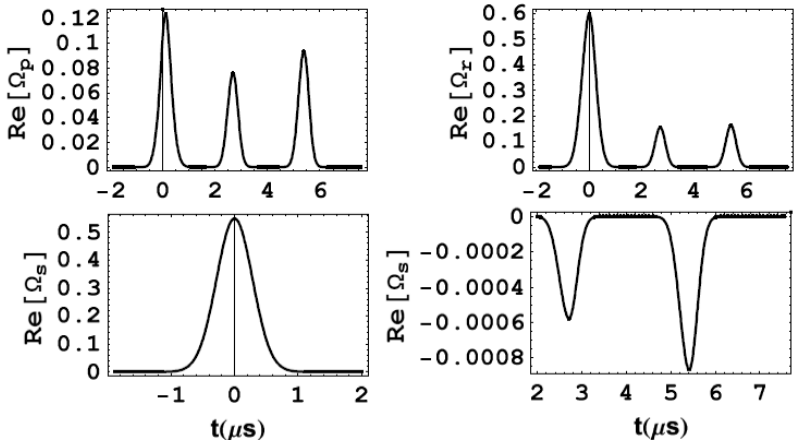

Fig. 13. The temporal dependence at $z = 10$ for the envelopes of the probe, drive, and switch pulses. The time is in μs.

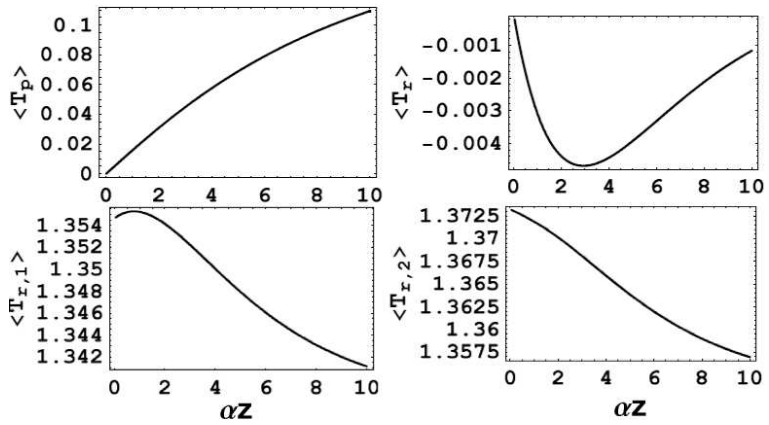

Fig. 14. Probe's time delay and the advancement of the drive as well as the generated restoring pulses in the drive channel are shown in the course of propagation. The time is in μs.

coherence gestured in Sect. 4. Last but not least, we have obtained the delay of the probe field whilst the drive shows advancement. The generated soliton train advances as depicted in Fig. 14. On assuming that $\alpha = 10^6$ m^{-1}, we can find that the instantaneous group velocity at $\alpha z = 10$ for the probe field is about 100 m/s whilst that for the generated pulses will be about 1 km/s. As those solitons obey the amplifier (or the attenuator) self-induced transparency (SIT) solitons, it is appreciated in a further study.

In the numerical solution to the coupled Maxwell–Bloch equations we have used the predictor-corrector as employed in [22].

8. Conclusion

We have established three-photon EIT with a prominent gain experienced by the drive field at the expense of the switch and probe fields for the scheme depicted in Fig. 1. The probe's absorption is attributed to the quantum switching effect. The drive field enhancement is shown to be exclusively due to the enhancement of the third- and fourth-rank components of the density matrix. The Rayleigh scattered light shows an exposed window with a small hole burnt into the spectrum. The space dependence of the spectrum shows for the strong field case that not only the drive is enhancing but also the switch field as well. The process is associated with considerable amount of information storage for moderate distances. We have employed the electromagnetically induced emission phenomenon to obtain soliton wave trains. The soliton train in the probe, drive, and switch channels propagates with shape preserving. Furthermore, the constituents of each soliton train do not overlap in time. By which we mean that these constituents in any channel do not override each other. These soliton trains are not only generated on the drive channel as has been designated but also in the switch channel revealing multiple--light storage phenomenon and as a consequence of the electromagnetically induced emission effect.

Acknowledgments

We are grateful to the Pomeranian University in Słupsk for financial support. The National Laboratory FAMO (UMK) in Toruń is acknowledged for partial financial support. We owe a special note of appreciation to the Referee for his encouragement.

References

[1] S.E. Harris, *Physics Today* **50**, 36 (1997).

[2] D.A. Braje, V. Balić, G.Y. Yin, S.E. Harris, *Phys. Rev A* **68**, 041801(R) (2003).

[3] S.E. Harris, Y. Yamamoto, *Phys. Rev. Lett.* **81**, 3611 (1998).

[4] S.E. Harris, Lene Vestergaard Hau, *Phys. Rev. Lett.* **82**, 4611 (1999).

[5] B.S. Ham, P.R. Hemmer, *Phys. Rev. Lett.* **84**, 4080 (2000).

[6] A. Zibrov, C.Y. Ye, Y.V. Rostovtsev, A.B. Matsko, M.O. Scully, *Phys. Rev. A* **65**, 043817 (2002).

[7] M. Yan, R.G. Rickey, Y. Zhu, *Phys. Rev A* **64**, 041801(R) (2001).

[8] A.S. Zibrov, M.D. Lukin, D.E. Nikonov, L. Holberg, M.O. Scully, V.L. Velichansky, H.G. Robinson, *Phys. Rev. Lett.* **75**, 1499 (1995).

[9] H. Kang, G. Hernandez, Y. Zhu, *Phys. Rev. A* **70**, 061804(R) (2004).

[10] H. Kang, G. Hernandez, Y. Zhu, *Phys. Rev. A* **70**, 011801(R) (2004).

[11] A.M. Alhasan, J. Fiutak, *Radiat. Phys. Chem.* **68**, 37 (2003).

[12] A.M. Alhasan, J. Fiutak, in: *IV Workshop on Atomic and Molecular Physics*, Ed. J. Heldt, Vol. 5258, SPIE – The International Society for Optical Engineering, 2003, p. 136.

[13] A.M. Alhasan, J. Fiutak, *Acta Phys. Pol. A* **109**, 143 (2006).

[14] A.M. Alhasan, J. Fiutak, *J. Mod. Opt.* **49**, 157 (2002).

[15] V.V. Yashchuk, D. Budker, W. Gawlik, D.F. Kimball, Yu. Malakyan, S.M. Rochester, *Phys. Rev. Lett.* **90**, 253001 (2003).

[16] B. Łobodziński, W. Gawlik, *Phys. Rev. A* **54**, 2238 (1996).

[17] J. Fiutak, J. Van Kranendonk, *J. Phys. B, At. Mol. Phys.* **13**, 2869 (1980).

[18] K. Blum, *Density Matrix Theory and Applications*, Plenum, New York 1981.

[19] R.G. Breene, Jr., *Theories of Spectral Line Shape*, Wiley, New York 1981.

[20] S. Dangel, R. Holzner, *Phys. Rev. A* **56**, 3937 (1997).

[21] A.D. Greentree, T.B. Smith, S.R. de Echaniz, A.V. Durrant, J.P. Marangos, D.M. Segal, J.A. Vaccaro, *Phys. Rev. A* **65**, 053802 (2002).

[22] A. Icsevgi, W.E., Lamb Jr., *Phys. Rev.* **185**, 517 (1969).